



Ultra-low friction and edge-pinning effect in large-lattice-mismatch van der Waals heterostructures

Mengzhou Liao^{1,2}, Paolo Nicolini², Luojun Du^{1,3}, Jiahao Yuan^{1,4}, Shuopei Wang^{1,5}, Hua Yu^{1,4}, Jian Tang^{1,4}, Peng Cheng⁶, Kenji Watanabe⁷, Takashi Taniguchi⁷, Lin Gu^{1,4}, Victor E. P. Claerhout², Andrea Silva⁸, Denis Kramer^{1,8,9}, Tomas Polcar^{2,8}, Rong Yang^{1,5}, Dongxia Shi^{1,4,5} and Guangyu Zhang^{1,4,5}✉

Two-dimensional heterostructures are excellent platforms to realize twist-angle-independent ultra-low friction due to their weak interlayer van der Waals interactions and natural lattice mismatch. However, for finite-size interfaces, the effect of domain edges on the friction process remains unclear. Here we report the superlubricity phenomenon and the edge-pinning effect at MoS₂/graphite and MoS₂/hexagonal boron nitride van der Waals heterostructure interfaces. We found that the friction coefficients of these heterostructures are below 10⁻⁶. Molecular dynamics simulations corroborate the experiments, which highlights the contribution of edges and interface steps to friction forces. Our experiments and simulations provide more information on the sliding mechanism of finite low-dimensional structures, which is vital to understand the friction process of laminar solid lubricants.

Friction causes massive energy dissipation and mechanical abrasion between machine component parts in the world every year (costing approximately 119 EJ)^{1,2}. Understanding the mechanism of the frictional processes and searching for an optimum material combination, ideally to provide a near-frictionless state, are thus essential. The concept of superlubricity was proposed by Shinjo and Hirano in the 1990s³, which describes the phenomenon of vanishing friction between two contact surfaces (also later known as structural lubricity). Superlubricity has been widely found in van der Waals (vdW) materials, as their crystalline structures are kept together by weak vdW forces⁴. However, superlubricity in two-dimensional (2D) homostructures shows a strong twist-angle dependence⁵⁻⁷. Layers prefer to rotate and lock in the commensurate state when sliding occurs, which leads to the disappearance of superlubricity^{6,8}. vdW heterojunctions may reduce the commensuration problem as the lattice mismatch between the two contact materials comes into play. Microscale superlubricity has been uncovered in the graphene/hexagonal boron nitride (h-BN) heterostructure with a significant reduction of twist-angle dependence⁹⁻¹³. However, the twist-angle dependence is still present in the graphene/h-BN heterostructure, perhaps due to the small lattice mismatch. Thus, it is crucial to explore the lattice mismatch influence on the superlubricity of 2D heterostructures. Furthermore, the effect of widespread domain edges and interface steps on the superlubricity of the finite-size 2D interfaces may prevent superlubricity.

In this work, we characterized 2D heterojunction interfaces with different lattice mismatches (MoS₂/graphite, MoS₂/h-BN

and graphene/h-BN) by lateral force atomic force microscopy (AFM). Our results show that the coefficient of friction (COF) of the large-lattice-mismatch MoS₂/graphite and MoS₂/h-BN heterojunction interfaces is below 10⁻⁶, and the twist-angle dependence is suppressed. We demonstrated that the friction forces of these two heterojunctions are dominated by pinned edges or substrate step effects rather than by resistance to interface sliding from, for example, potential energy corrugation. For comparison, interface sliding resistance dominates the friction process in the sliding of graphene/h-BN with a small lattice-mismatch. Classical molecular dynamics (MD) simulations indicate that atoms near the edges of the flake play a distinctive role during the sliding dynamics, as they present enhanced out-of-plane structural distortions with respect to the rest of the flake. Given the non-reactive nature of the force fields employed in the MD simulations, we also indirectly prove that dangling bonds at the edge of the domains contribute mostly to the friction force observed in climbing substrate steps.

Growth and characterization of vdW heterostructures

vdW heterostructure samples investigated in this work include MoS₂/graphite, MoS₂/h-BN and graphene/h-BN with lattice mismatches of 26.8, 24.6 and 1.8%, respectively. Figure 1a–c shows the structures of these three heterostructures. All the samples were prepared by an epitaxial growth technique described in our previous works¹⁴⁻¹⁶ (see Methods for more details). Figure 1d–f shows typical AFM topographic images; these epitaxial interfaces are ultraclean. The heights of monolayer MoS₂ on graphite and

¹Beijing National Laboratory for Condensed Matter Physics and Institute of Physics, Chinese Academy of Sciences, Beijing, China. ²Department of Control Engineering, Faculty of Electrical Engineering, Czech Technical University in Prague, Prague, Czech Republic. ³Department of Electronics and Nanoengineering, Aalto University, Tietotie, Finland. ⁴School of Physical Sciences, University of Chinese Academy of Sciences, Beijing, China. ⁵Songshan Lake Materials Laboratory, Dongguan, China. ⁶Oxford Instruments (Shanghai) Co. Limited, Shanghai, China. ⁷National Institute for Materials Science, Tsukuba, Japan. ⁸National Centre for Advanced Tribology (nCATS), Department of Mechanical Engineering, University of Southampton, Southampton, UK. ⁹Faculty of Mechanical Engineering, Helmut Schmidt University, Hamburg, Germany. ✉e-mail: gyzhang@iphy.ac.cn

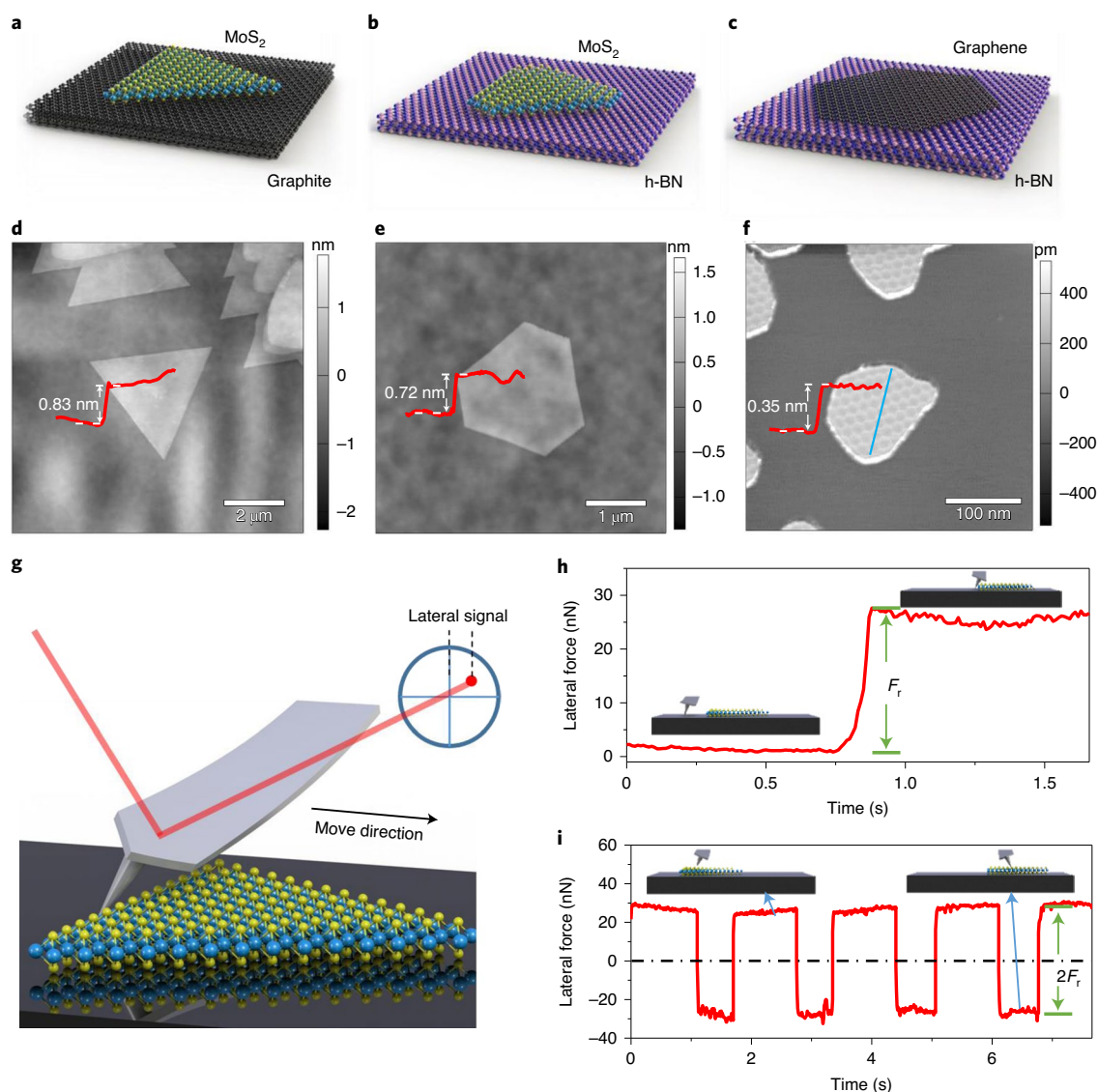


Fig. 1 | Friction characterizations of 2D heterostructures. **a–f**, Atomic structures (**a–c**) and AFM images (**d–f**) of the three heterostructures MoS₂/graphite (**a,d**), MoS₂/h-BN (**b,e**) and graphene/h-BN (**c,f**). **g**, Schematic of the measurement process for friction forces. **h,i**, Two different strategies for the friction force characterizations of MoS₂/graphite and MoS₂/h-BN heterostructures, by pushing from the edge of the domain (**h**) or by dragging with the tip placed at the centre of the domain (**i**); the sign of the force indicates the sliding direction.

h-BN were 0.83 and 0.72 nm, respectively, and the height of monolayer graphene on h-BN is 0.35 nm; all are in agreement with previous reports^{16,17}. The arithmetic mean deviation of the assessed profiles of the substrate surfaces in Fig. 1d–f were 0.17, 0.13 and 0.02 nm, respectively, which suggests atomically flat substrate surfaces and excludes the influence of the substrate roughness in the following experiments. We used selected area electron diffraction to characterize the lattice alignment of our MoS₂/graphite and MoS₂/h-BN heterostructures. As illustrated in Supplementary Fig. 1b(e), the hexagonal diffraction spots of both MoS₂ and graphite (h-BN) had the same orientation, which indicates either a 0° or 60° twisting angle between the as-grown MoS₂ and graphite (h-BN) substrate. Supplementary Fig. 1h shows that the period of the moiré superlattice of the as-grown graphene/h-BN heterostructure was ~16 nm, which also suggests a 0° twist angle. The Raman and photoluminescence spectra in Supplementary Fig. 1c,f also demonstrate a high sample quality (or more information, refer to Supplementary Note 1).

Superlubricity behaviour of vdW heterostructures

We performed friction force measurements by AFM in a dry N₂ atmosphere to reduce contamination from the air (see Supplementary Note 10 for the discussion of the absorbed contaminations). Figure 1d–f and Supplementary Fig. 2 show that the thickness of our samples is homogeneous and the actual values indicate monolayer-thick samples, which exclude the presence of contamination. Figure 1g shows a schematic of our measurements process. Based on a manipulation technique we developed previously^{11,18}, we can slide atop epitaxial domains on the substrate by using an AFM tip and monitor the lateral force during the sliding simultaneously (see Methods and Supplementary Note 2 for more details). In the experiments, we explored two approaches to slide on-top domains on substrates by using AFM tips. The first is illustrated in Fig. 1h, in which we laterally pushed the edge of the top domain and detected the difference in lateral force before and after the on-top domain sliding. The second approach is shown in Fig. 1i. For the MoS₂/graphite and MoS₂/h-BN heterostructures, we could slide the

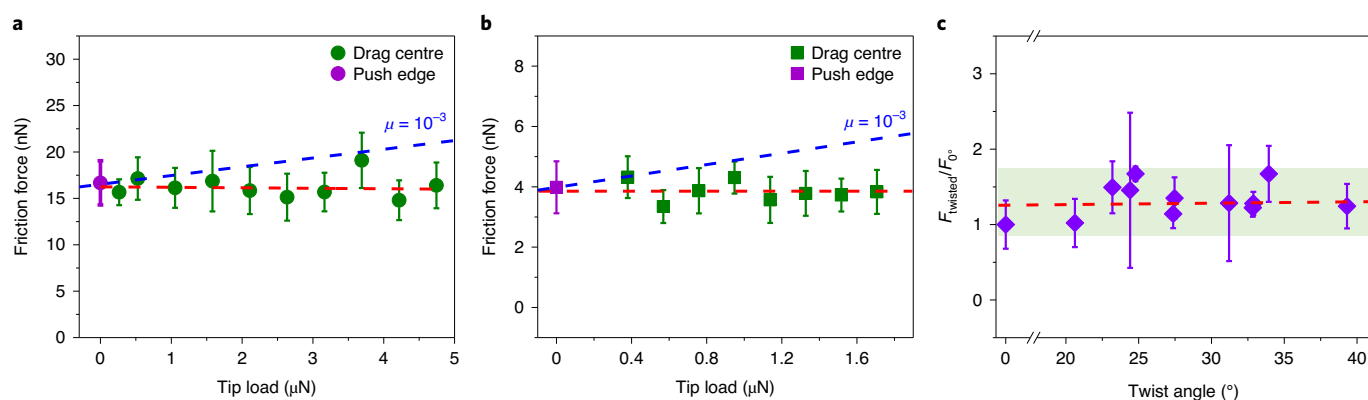


Fig. 2 | Superlubricity of MoS₂/graphite and MoS₂/h-BN heterostructure interfaces. **a,b**, Friction force as a function of the tip load of MoS₂/graphite (**a**) and MoS₂/h-BN (**b**) heterostructures, obtained by AC200TS and AC240TS tips under a N₂ gas environment. The red dashed lines are the fittings of all the data points in **a** and **b**; the blue dashed lines show the limit of superlubricity. **c**, Normalized friction force as a function of the twist angle of the MoS₂/graphite heterostructure. F_0 and F_{twisted} are the friction forces of a MoS₂ domain before (aligned) and after twisting. The red dashed line is the fit. Error bars are the standard deviation (s.d.) of the data points.

top domains back and forth laterally by engaging the tip onto the centre of the domain, with a load that ranged from 0.4 to 5 μN, as the friction force between the tip and MoS₂ is much greater than that between MoS₂ and graphite (or h-BN).

According to Amontons's law, the dependence of the friction force F_r on the load L is expressed by:

$$F_r = \mu L,$$

where μ is the COF. By taking advantage of both approaches, we can change the applied tip load L_{tip} from zero to a few micronewtons (a near-zero tip load is achieved by pushing the edge). The normal force experienced by the flake can be decomposed into two contributions:

$$L = L_0 + L_{\text{tip}},$$

with L_0 being the adhesion between MoS₂ and graphite (or h-BN) and L_{tip} the load applied to the tip. It follows that:

$$F_r = \mu (L_0 + L_{\text{tip}}) = \mu L_0 + \mu L_{\text{tip}} = F_{r0} + \mu L_{\text{tip}}.$$

As shown in Fig. 2a,b, under N₂ the friction forces of the aligned MoS₂/graphite and MoS₂/h-BN heterostructures are almost the same for different values of L_{tip} , which indicates a constant F_{r0} and ultra-low COF. As shown in Fig. 2, the COF of both aligned MoS₂/graphite and MoS₂/h-BN heterostructure interfaces is well below 10⁻³, which is considered the threshold for superlubricity¹⁹. To calculate the friction coefficient precisely from the slope in Fig. 2a,b, a much higher resolution and noise reduction of the AFM signal is needed.

We can also use an alternative approach to estimate the COF. The adhesive force between MoS₂ domains and graphite or h-BN represents the major contribution to the load L (ref. 7). Thus, we can estimate the magnitude of the COF, μ , by using:

$$\mu = F_{r0}/L_0$$

$$L_0 = GA$$

where $G = 1.13$ GPa is the adhesive pressure between graphite and the MoS₂ sheets²⁰ and A is the area of the domain. From Supplementary Fig. 3a, the area of our largest MoS₂ domain on

graphite is 15.00 μm², which gives an adhesive force L_0 of 16.95 mN. The corresponding friction force F_{r0} is 44.15 nN, and the COF of the aligned MoS₂/graphite heterostructure interfaces is 2.60×10^{-6} . This value is almost two orders of magnitude smaller than those reported in previous studies^{7,21,22}. For the aligned MoS₂/h-BN heterostructure, according to Supplementary Fig. 3b, the COF value is around 2.29×10^{-6} , similar to that MoS₂/graphite.

To further explore the twist-angle dependence of superlubricity in heterostructures with a large lattice mismatch, we performed friction tests on the MoS₂/graphite heterostructure with different twist angles. Although the heterostructures can be rotated to any twist angle¹⁸, they are only stable at large twist angles during sliding. We compared the friction force between aligned structures (0° or 60°) and large twist angles of different MoS₂ domains. As shown in Fig. 2c, the measured friction forces from the MoS₂/graphite heterostructures before and after twisting show no significant angular dependence. This phenomenon is due to the fact that the in-plane interface friction force is almost zero even at 0° due to incommensurability, and the influence of the twist angle on the friction force has a negligible contribution to the total friction force (see Supplementary Note 3 for more details).

Edge-pinning effect of vdW heterostructures

Although the interface COFs of aligned MoS₂/graphite and MoS₂/h-BN heterostructure interfaces are small, there is still a constant friction force F_{r0} independent of load within the normal load range considered. Previous results pointed out that the friction force could be affected by many parameters, such as edges, interface steps and contaminations^{23–25}. To determine the origin of this constant friction force, we defined two parameters: shear strength S and domain edge-pinning strength E . Given the finite size of our samples, S and E are defined as follows:

$$S = F_r/A$$

$$E = F_r/P,$$

where P is the perimeter of domains. We can expect three situations: (1) the in-plane interface sliding resistance contributes predominantly to the friction force and S is thus constant with respect to the area of the domains; (2) the in-plane interface friction is negligible and the edge-pinning effect dominates the friction process and E is constant with respect to the perimeter of the domains; or (3) both

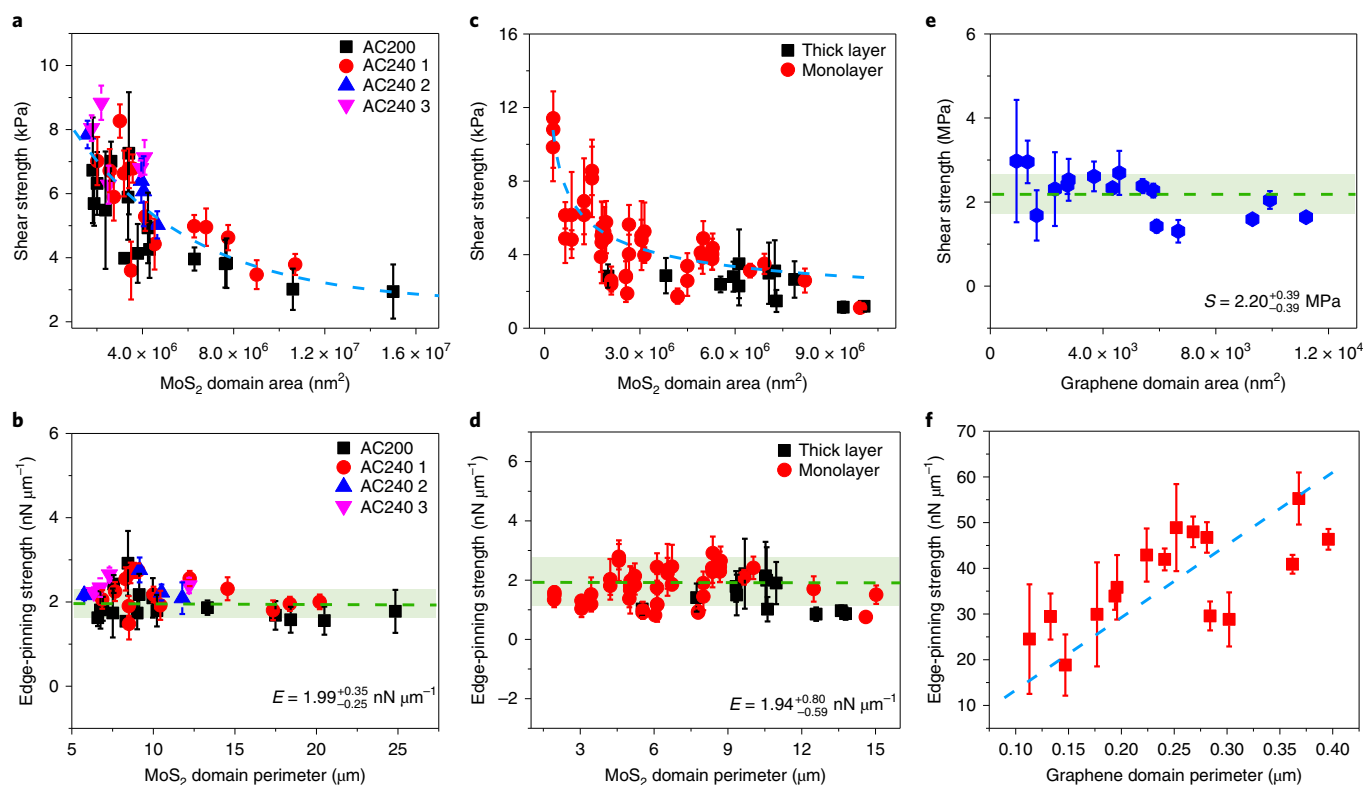


Fig. 3 | Source of friction for three different heterostructure interfaces. a, b, Plots of the friction characterization of MoS₂/graphite as a function of the total domain area (**a**) and total perimeter (**b**). AC240 1–3 mark the data from three different AC240 tips. **c, d,** Similar plots for the domain area (**c**) and perimeter (**d**) of MoS₂/h-BN. **e, f,** Friction characterization of graphene/h-BN as a function of the domain area (**e**) and perimeter (**f**). Dashed lines are linear fits. Error bars are the s.d. of the data points.

effects contribute significantly to the friction force so both S and E cannot be constant.

We first measured the friction force of the aligned heterostructure samples with various contact areas under a dry N₂ atmosphere. The results are consistent even when different tips were used (Supplementary Fig. 3), which suggests a good consistency and repeatability of our calibration method. Figure 3a shows a plot of the shear strength of the aligned MoS₂/graphite heterostructure as a function of the domain area, which clearly reveals a non-constant profile. In contrast, when we plot the data as E versus P , as shown in Fig. 3b, the edge-pinning strength is constant, with $E = 1.99^{+0.35}_{-0.25} \text{ nN } \mu\text{m}^{-1}$. These results indicate that the interface (in-plane) friction within aligned MoS₂/graphite is negligible, and the edges of the MoS₂ domains are pinned to the surface of graphite. Aligned MoS₂/h-BN exhibits a similar behavior, as shown in Fig. 3c,d, where $E = 1.94^{+0.80}_{-0.59} \text{ nN } \mu\text{m}^{-1}$ is very close to that of MoS₂/graphite. It is also worth noting that the thickness of the MoS₂ domains have no apparent effect on the friction force due to the negligible interface friction (refer to Supplementary Fig. 2d). All the edges of the MoS₂ domains in our experiment have the same zigzag direction (supported by Supplementary Figs. 1 and 5). So here E is actually the zigzag edge-pinning strength. As described above, the friction force of large-lattice-mismatch MoS₂/graphite and MoS₂/h-BN heterostructures mainly comes from the pinned edges. Therefore, the friction coefficients of edge-free, single-crystal MoS₂/graphite and MoS₂/h-BN heterostructure interfaces should be significantly lower than 10⁻⁶.

The behaviour of the aligned graphene/h-BN heterostructure, which has a small lattice mismatch (1.8%), is different from that of the MoS₂/graphite and MoS₂/h-BN heterostructures. From Fig. 3e,f, we can see that the shear strength of the graphene/h-BN

heterostructure is constant and equal to $2.20 \pm 0.39 \text{ MPa}$, which suggests that the in-plane interface friction is dominant. The dominance of in-plane friction in aligned graphene/h-BN can be understood given its near-commensurate nature at small twist angles, in which the period of moiré superlattice is larger than that in the MoS₂-based heterostructures^{16,26,27}. We must mention that the shear strength value of the graphene/h-BN heterostructure in our experiment is larger than that of Song et al.¹⁰. The reason for this discrepancy can be attributed to the different thicknesses of the graphene layers in the heterostructures, which can influence the sliding energy profile²⁸, the z -direction fluctuations and the structure of the moiré pattern²⁹. These properties eventually determine the interface friction force.

Simulation results of the edge-pinning effect

To understand the origin of the edge-pinning effect for the MoS₂/graphene heterostructure, we performed a set of MD simulations. The computational set-up is illustrated in Fig. 4a,b. We considered triangular zigzag-terminated MoS₂ flakes with different side lengths that ranged from approximately 2 to 20 nm. As no reactive force fields were available for the MoS₂/graphene system, we described the interlayer interactions by means of the Stillinger–Weber³⁰ and AIREBO³¹ potentials for MoS₂ and graphene, respectively. The interlayer interactions were modelled via a Lennard–Jones potential, recently parameterized by using ab initio data³². According to this potential, the adhesive pressure between MoS₂ and graphite is 1.20 GPa, which is in good agreement with both experiment and ab initio calculations²⁰. Supplementary Note 6 reports an extensive analysis using density functional theory calculations that shows no chemical bonding between the MoS₂ edges and the graphene substrate, which justifies the use of a non-reactive force field. Moreover,

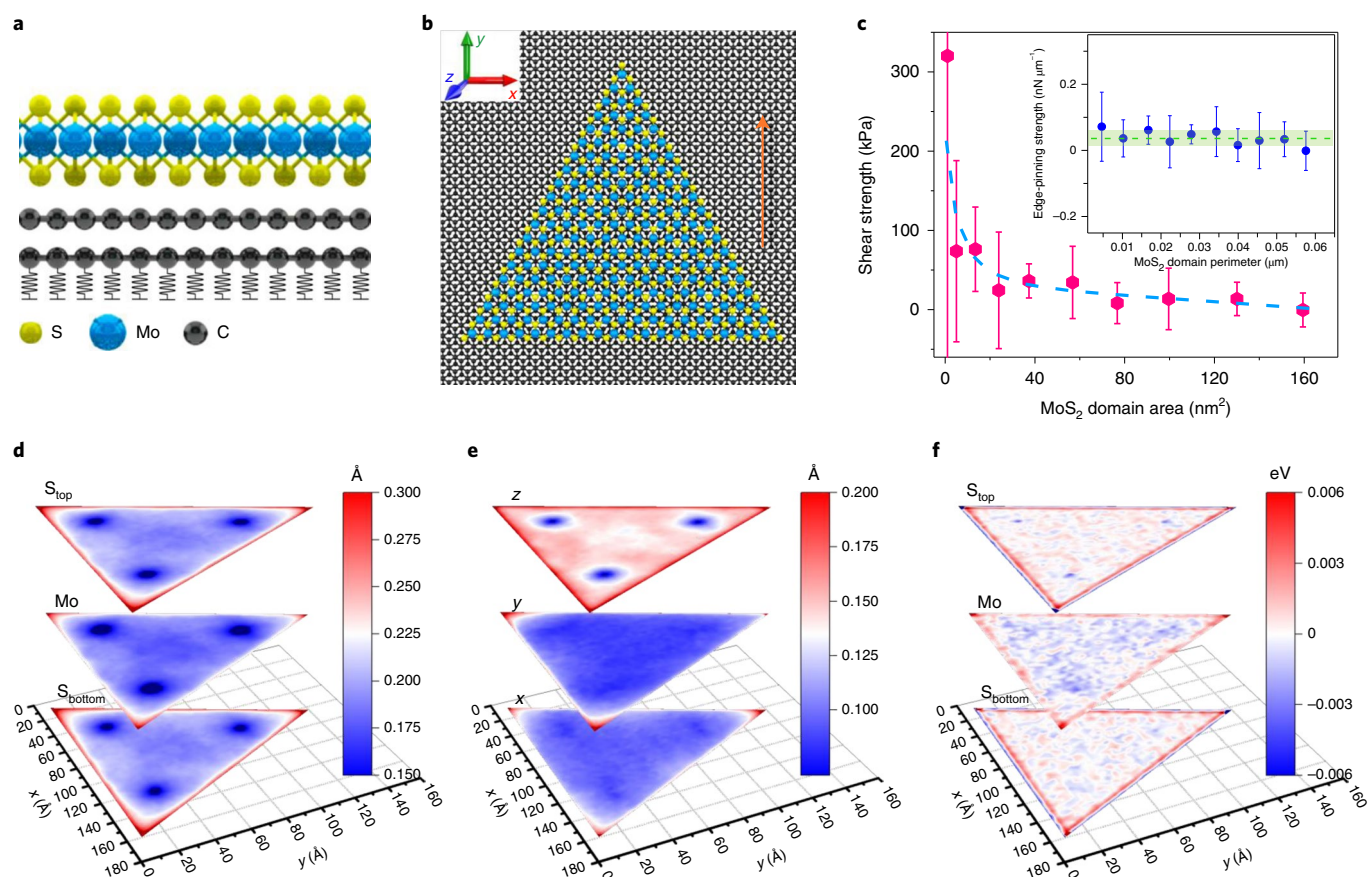


Fig. 4 | MD simulation results of MoS₂ flakes sliding on graphite. **a, b**, Side (**a**) and top (**b**) views of the MD computational set-up. **c**, Calculated shear strength as a function of the MoS₂ flake area. Inset: calculated edge-pinning strength as a function of the MoS₂ flake perimeter. Dashed lines are the fits. Error bars are the s.d. of the data points, and the error bar of the shear strength of the smallest flake is 467.64 kPa. **d**, r.m.s.d. maps of different atomic layers in the MoS₂ flake calculated with respect to the optimized geometry for a typical trajectory (flake size ~16 nm). **e**, Maps of the r.m.s.d. calculated on the three Cartesian components separately, and for the bottom S atoms only (for the maps of the other atomic layers, see Supplementary Note 9). **f**, Per-atom average potential energy fluctuation maps of different atomic layers in the MoS₂ flake. The three bright spots in **e** mark the position of the fixed atoms (see Methods for more details). For the potential energy, values are reported as the difference with respect to the mean value.

the sliding potential induced by the Lennard–Jones coupling was benchmarked against density functional theory calculations in a small test system. The classical force field captures the shape of the potential energy surface, but it slightly underestimates the barrier height, as shown in Supplementary Note 7. Thus, we expect the simulation to correctly reproduce the trends found in the experiments, albeit scaled. All the systems were equilibrated at room temperature, after which non-equilibrium simulations were performed by applying a constant speed protocol and calculating the lateral force that acts on the flake (more details in Methods).

Figure 4 summarizes the simulation results. The shear and edge-pinning strengths are reported as functions of the MoS₂ domain area and perimeter, respectively. As shown in Fig. 4c, the shear strength presents a decreasing profile as A increases, and E is almost constant. We also calculated the shear strength of an infinite heterostructure, $S_{\text{infinite}} = 1.38$ kPa, which is at least one order of magnitude smaller than that of our finite heterostructures. These trends are consistent with the experimental observations. For a more in-depth insight into the underlying mechanisms, we analysed the results in terms of structural and energy parameters. Figure 4d reports the map of the atomic root mean square displacement (r.m.s.d.) with respect to the equilibrium positions for different atomic layers of MoS₂, and averaged over the MD trajectory. The mean displacement of edge atoms is significantly larger than that

for centre atoms. Data distributions of the edge and centre regions (Supplementary Fig. 4a) also show that edge atoms (particularly for atoms at the edge and at one lattice distance from it) have both a larger peak r.m.s.d. value and a broader distribution. Moreover, from Fig. 4e it is possible to notice that the main contribution to the r.m.s.d. comes from the out-of-plane atomic distortions (see Supplementary Note 9 for the maps related to the other atomic layers). Potential energy maps of different atomic types within the MoS₂ layer (Fig. 4f) show that the edge S atoms present a distinct behavior in terms of potential energy than the centre S atoms. In particular, S atoms located at the edge are more mobile than central atoms due to the lower coordination and thus are more prone to be trapped in the energy minima of the substrate, which leads to the edge-pinning effect. Edge Mo atoms also present differences with respect to the central ones, but the behaviour is not as significant as that for S atoms (see the potential energy data in Supplementary Fig. 4b,c for a more detailed discussion).

The MD simulations indicate that, during sliding, the dynamics of the edge atoms present peculiar traits for distortions and potential energy fluctuations, which ultimately provide the greatest contribution to the friction force. Indeed, high-resolution transmission electron microscopy (TEM) (Supplementary Fig. 5) shows more pronounced lattice distortions at the edges, which supports the simulation results.

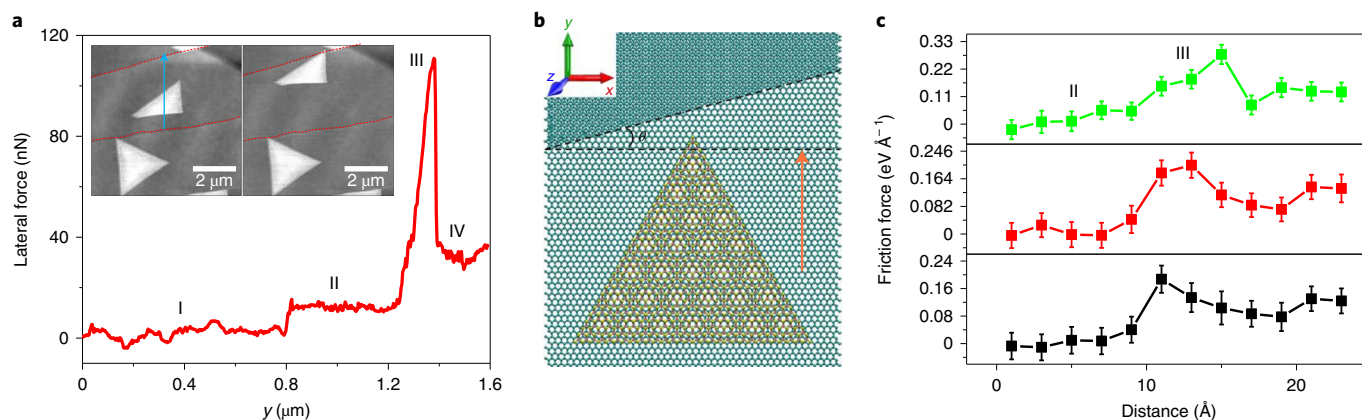


Fig. 5 | Effects of interface steps on friction force. **a**, Lateral force measurement when pushing one MoS₂ domain across a monolayer step of graphite. I, II, III and IV mark the different stages of the tip movement: I, the tip is moving on graphite; II, the tip is pushing the MoS₂ domain; III, the MoS₂ domain is moving across the step of graphite; IV, the MoS₂ domain locks on the step and the tip jumps onto the MoS₂ surface. Inset: in the AFM image the red dashed line marks the graphite step, and the blue arrow shows the tip route. **b**, MD computational set-up. The dashed line marks the graphite step and the orange arrow marks the direction normal to the sliding direction. **c**, Average friction force experienced by the MoS₂ flake as a function of the distance travelled at 16° (top), 6° (middle) and 0° (bottom). II and III tags mark the same stages as in **a**.

Step-pinning effect in MoS₂/graphite heterostructure

We found experimentally that substrate steps can impede the sliding of MoS₂ domains even when they only have the height of a graphene monolayer (~0.4 nm). As shown in Fig. 5a and Supplementary Video 1, when we pushed a MoS₂ domain across a graphite step edge, we observed various resistance forces during different stages (I, II, III, IV). Stage III represents the MoS₂ domain crossing the step of graphite and finally locking on it. The resistance force increases almost tenfold before the MoS₂ domain locks on the graphite step. Here we define the interface step-pinning strength P_{IS} as:

$$P_{IS} = F_{\max}/d$$

where F_{\max} is the maximum force of stage III and d is the length of the step edge under the MoS₂ domain. The interface step pinning strength in Fig. 5a is $P_{IS} \approx 100 \text{ nN } \mu\text{m}^{-1}$, which is two orders of magnitude larger than the edge-pinning strength mentioned above. Therefore, the friction force rises dramatically if interface steps are present. We also used MD simulations to monitor the friction force when a MoS₂ flake is pushed towards a graphite step at different angles with respect to the sliding direction, as shown in Fig. 5b,c and Supplementary Video 2. From Fig. 5c, we can see that, regardless of the orientation of the step, all the profiles show a qualitatively similar behaviour; the friction force will rise several times when the MoS₂ layer approaches the step. However, this increase in friction force is smaller than that observed in experiments. The difference between simulations and experiments can be ascribed to the fact that our model accounts only for non-bonded vdW interactions between the flake and substrate (that is, the model does not allow the formation of chemical bonds between MoS₂ and graphene atoms). Previous works show that chemical bonds on graphite steps have a strong influence on the friction force³³, so we attribute the step-pinning effect to the interaction between the MoS₂ layer and the free chemical bonds on the graphite step.

Conclusions

In conclusion, we demonstrated that large-lattice-mismatch MoS₂/graphite and MoS₂/h-BN heterojunction interfaces provide ultra-low coefficients of friction, $\sim 10^{-6}$, without any twist-angle dependence. Both experiments and MD calculations indicated that the pinned edges and interface steps in MoS₂/graphite and MoS₂/h-BN heterojunctions dominate the friction process, whereas

the small lattice mismatch in graphene/h-BN results in a significant contribution to the interface friction. Our results show that the large lattice mismatch of two contact surfaces and the absence of interface steps are key components to the design of a near-frictionless sliding pair.

Online content

Any methods, additional references, Nature Research reporting summaries, source data, extended data, supplementary information, acknowledgements, peer review information; details of author contributions and competing interests; and statements of data and code availability are available at <https://doi.org/10.1038/s41563-021-01058-4>.

Received: 20 October 2020; Accepted: 21 June 2021;

Published online: 05 August 2021

References

- Holmberg, K., Andersson, P. & Erdemir, A. Global energy consumption due to friction in passenger cars. *Tribol. Int.* **47**, 221–234 (2012).
- Holmberg, K. & Erdemir, A. Influence of tribology on global energy consumption, costs and emissions. *Friction* **5**, 263–284 (2017).
- Shinjo, K. & Hirano, M. Dynamics of friction—superlubric state. *Surf. Sci.* **283**, 473–478 (1993).
- Geim, A. K. & Grigorieva, I. V. Van der Waals heterostructures. *Nature* **499**, 419–425 (2013).
- Dienwiebel, M. et al. Superlubricity of graphite. *Phys. Rev. Lett.* **92**, 126101 (2004).
- Zheng, Q. et al. Self-retracting motion of graphite microflakes. *Phys. Rev. Lett.* **100**, 067205 (2008).
- Li, H. et al. Superlubricity between MoS₂ monolayers. *Adv. Mater.* **29**, 1701474 (2017).
- Filippov, A. E., Dienwiebel, M., Frenken, J. W., Klafter, J. & Urbakh, M. Torque and twist against superlubricity. *Phys. Rev. Lett.* **100**, 046102 (2008).
- Ribeiro-Palau, R. et al. Twistable electronics with dynamically rotatable heterostructures. *Science* **361**, 690–693 (2018).
- Song, Y. et al. Robust microscale superlubricity in graphite/hexagonal boron nitride layered heterojunctions. *Nat. Mater.* **17**, 894–899 (2018).
- Wang, D. et al. Thermally induced graphene rotation on hexagonal boron nitride. *Phys. Rev. Lett.* **116**, 126101 (2016).
- Leven, I., Krepel, D., Shemesh, O. & Hod, O. Robust superlubricity in graphene/h-BN heterojunctions. *J. Phys. Chem. Lett.* **4**, 115–120 (2013).
- Mandelli, D., Leven, I., Hod, O. & Urbakh, M. Sliding friction of graphene/hexagonal-boron nitride heterojunctions: a route to robust superlubricity. *Sci. Rep.* **7**, 10851 (2017).
- Yu, H. et al. Precisely aligned monolayer MoS₂ epitaxially grown on h-BN basal plane. *Small* **13**, 1603005 (2017).

15. Du, L. J. et al. Modulating PL and electronic structures of MoS₂/graphene heterostructures via interlayer twisting angle. *Appl. Phys. Lett.* **111**, 26310 (2017).
 16. Yang, W. et al. Epitaxial growth of single-domain graphene on hexagonal boron nitride. *Nat. Mater.* **12**, 792–797 (2013).
 17. Radisavljevic, B., Radenovic, A., Brivio, J., Giacometti, V. & Kis, A. Single-layer MoS₂ transistors. *Nat. Nanotechnol.* **6**, 147–150 (2011).
 18. Liao, M. et al. Twist angle-dependent conductivities across MoS₂/graphene heterojunctions. *Nat. Commun.* **9**, 4068 (2018).
 19. Müser, M. H. in *Fundamentals of Friction and Wear on the Nanoscale* (eds Gnecco, E. & Meyer, E.) 209–232 (Springer International, 2015).
 20. Li, B. et al. Probing van der Waals interactions at two-dimensional heterointerfaces. *Nat. Nanotechnol.* **14**, 567–572 (2019).
 21. Martin, J. M., Donnet, C., Lemogne, T. & Epicier, T. Superlubricity of molybdenum-disulfide. *Phys. Rev. B* **48**, 10583–10586 (1993).
 22. Berman, D., Deshmukh, S. A., Sankaranarayanan, S. K., Erdemir, A. & Sumant, A. V. Macroscale superlubricity enabled by graphene nanoscroll formation. *Science* **348**, 1118–1122 (2015).
 23. Dietzel, D., Feldmann, M., Schwarz, U. D., Fuchs, H. & Schirmeisen, A. Scaling laws of structural lubricity. *Phys. Rev. Lett.* **111**, 235502 (2013).
 24. de Wijn, A. S. (In)commensurability, scaling, and multiplicity of friction in nanocrystals and application to gold nanocrystals on graphite. *Phys. Rev. B* **86**, 085429 (2012).
 25. Muser, M. H., Wenning, L. & Robbins, M. O. Simple microscopic theory of Amontons's laws for static friction. *Phys. Rev. Lett.* **86**, 1295–1298 (2001).
 26. Yankowitz, M. et al. Emergence of superlattice Dirac points in graphene on hexagonal boron nitride. *Nat. Phys.* **8**, 382–386 (2012).
 27. Wang, E. et al. Gaps induced by inversion symmetry breaking and second-generation Dirac cones in graphene/hexagonal boron nitride. *Nat. Phys.* **12**, 1111–1116 (2016).
 28. Gao, W. & Tkatchenko, A. Sliding mechanisms in multilayered hexagonal boron nitride and graphene: the effects of directionality, thickness, and sliding constraints. *Phys. Rev. Lett.* **114**, 096101 (2015).
 29. Mandelli, D., Ouyang, W., Urbakh, M. & Hod, O. The princess and the nanoscale pea: long-range penetration of surface distortions into layered materials stacks. *ACS Nano* **13**, 7603–7609 (2019).
 30. Ding, Z. W., Pei, Q. X., Jiang, J. W., Huang, W. X. & Zhang, Y. W. Interfacial thermal conductance in graphene/MoS₂ heterostructures. *Carbon* **96**, 888–896 (2016).
 31. Brenner, D. W. et al. A second-generation reactive empirical bond order (REBO) potential energy expression for hydrocarbons. *J. Phys. Condens. Matter* **14**, 783–802 (2002).
 32. Silva, A., Claerbout, V. E. P., Polcar, T., Kramer, D. & Nicolini, P. Exploring the stability of twisted van der Waals heterostructures. *ACS Appl. Mater. Inter.* **12**, 45214–45221 (2020).
 33. Chen, Z., Khajeh, A., Martini, A. & Kim, S. H. Chemical and physical origins of friction on surfaces with atomic steps. *Sci. Adv.* **5**, eaaw0513 (2019).
- Publisher's note** Springer Nature remains neutral with regard to jurisdictional claims in published maps and institutional affiliations.
- © The Author(s), under exclusive licence to Springer Nature Limited 2021

Methods

Sample preparation. MoS₂ domains were grown by three-temperature-zone chemical vapour deposition. S (Alfa Aesar, 99.9%, 4 g) and MoO₃ (Alfa Aesar, 99.999%, 50 mg) powders were used as sources, loaded separately in two inner tubes and placed at zone I and zone II, respectively. Substrates were loaded in zone III. During the growth, Ar/O₂ (gas flow rate, 75/3 sccm) was flowed as the carrying gases and temperatures for the S source, MoO₃ source and wafer substrate were 115, 530 and 930 °C, respectively. In this experiment, graphite and h-BN substrates were mechanically exfoliated from highly ordered pyrolytic graphite, graphenium graphite (Manchester Nanomaterials) and bulk h-BN.

Plasma-enhanced chemical vapour deposition growth of the graphene/h-BN heterostructure. h-BN flakes were prepared by mechanical exfoliation of h-BN crystals onto 300 nm SiO₂/Si substrate by Scotch tape (3M). Before growth, the substrate was annealed in hydrogen at 400 °C for 30 min to remove tape residues. Subsequently, the epitaxial growth was carried out by plasma-enhanced chemical vapour deposition at a substrate temperature of ~500 °C with pure CH₄ as the carbon source, and the gas pressure and plasma power were 0.2 torr and 100 W, respectively. The growth period was about 1.5 h.

Sample characterizations. AFM measurements were performed on an Asylum Research Cypher S with AC240TS-R3 and AC200TS-R3 tips. Photoluminescence and Raman characterizations were performed in a Horiba Jobin Yvon LabRAM HR-Evolution Raman system. The laser wavelength was 532 nm. Selected area electron diffraction was performed in a TEM (Philips CM200) operated at 200 kV (see Supplementary Note 1 for the characterization results).

Environment control and cantilever calibration. We placed Cypher S in a specialized glove box. Under dry N₂ conditions, O₂ and H₂O were below 0.5 ppm, and the pressure of the glove box was set to 4 mbar. During the experiment, the temperature inside the Cypher cabinet was 35 ± 1 °C. We used the standard Sader's method to calibrate the cantilever in the vertical direction and a non-contact method for the lateral direction^{34,35}. During our measurements, two types of silicon AFM tips (see above) with different spring constants were used. The velocity of the tips was 0.6 μm s⁻¹. For more details, see Supplementary Note 2.

MD simulations. Crystal structures for MoS₂ (ref. ³⁶) and graphite³⁷ were retrieved from the Crystallography Open Database³⁸. The unit cell of bulk MoS₂ was transformed into a monolayer structure by removing half of the atoms in the cell and adding 20 Å of vacuum along the direction perpendicular to the basal plane to avoid interactions between images. The structure was replicated in the *a* and *b* directions and triangular flakes with zigzag edges (ending with S atoms) and varying sides were cut out. The flake structures were then optimized according to the Stillinger–Weber potential for MoS₂ (ref. ³⁹). A bilayer graphene structure was obtained in a similar way and then optimized using the AIREBO description³¹. The flake structures were then placed on top of the substrates within an orthogonal cell and finally optimized via an energy minimization with the conjugate gradient method. The interlayer interactions were modelled using solely a Lennard–Jones potential. As the parameterization available in the literature³⁰ proved to be unsuitable to describe the stacking interaction of MoS₂ and graphene correctly, we refined the actual parameters using density functional theory calculations as a reference. More details about the procedure can be found elsewhere³². All structures were then thermalized at 300 K for 50 ps using a Nosé–Hoover thermostat^{39,40}. To obtain results with statistical significance, ten independent runs were performed for each set-up by initializing the atomic velocities to the target temperature with different seeds for the random number generator. After this, sliding simulations of 2 ns were carried out by imposing a constant speed of 1 m s⁻¹ to three atoms (whose relative positions were not allowed to change) within the top S layer and equidistant from the corners of the flake. To prevent the whole system from moving, the positions of the C atoms that belonged to the bottommost graphene layer were tethered to their initial positions by applying harmonic potentials with a spring constant of 0.3 N m⁻¹. A verification of the validity of the results in the low-speed limit by means of quasistatic simulations is presented in Supplementary Note 8. During sliding, a Nosé–Hoover thermostat set to 300 K and with a damping constant of 100 time units was coupled to all non-rigid atoms. For the flake atoms, the temperature was computed after removing the velocity of the centre of mass of the flake. Forces that acted on the externally controlled group of atoms and along the sliding direction were stored and then averaged over the production trajectory. Final averages and standard deviations over the ten independent trajectories were then calculated and are reported in the main text. For the simulations that involved the graphitic step, to mimic the AFM set-up, the motion of the MoS₂ flake was obtained by imposing a constant speed to three atoms at the centre of the flake edge opposite the graphitic step. For all the MD

simulations, a time step of 0.2 fs was employed. All the calculations were carried out using the LAMMPS package⁴¹. The schematics of the computational set-up in Figs. 4 and 5 were obtained using VMD software⁴².

Data availability

The authors declare that the data supporting the findings of this study are available within the paper and its Supplementary information files. Source data are provided with this paper.

References

- Sader, J. E., Chon, J. W. M. & Mulvaney, P. Calibration of rectangular atomic force microscope cantilevers. *Rev. Sci. Instrum.* **70**, 3967–3969 (1999).
- Wagner, K., Cheng, P. & Vezenov, D. Noncontact method for calibration of lateral forces in scanning force microscopy. *Langmuir* **27**, 4635–4644 (2011).
- Schonfeld, B., Huang, J. J. & Moss, S. C. Anisotropic mean-square displacements (MSD) in single-crystals of 2H-MoS₂ and 3R-MoS₂. *Acta Crystallogr. B* **39**, 404–407 (1983).
- Zemann, J. Crystal structures. Vol. 1 by R. W. G. Wyckoff. *Acta Crystallogr.* **18**, 139–139 (1965).
- Grazulis, S. et al. Crystallography Open Database (COD): an open-access collection of crystal structures and platform for world-wide collaboration. *Nucleic Acids Res.* **40**, D420–D427 (2012).
- Nose, S. A unified formulation of the constant temperature molecular-dynamics methods. *J. Chem. Phys.* **81**, 511–519 (1984).
- Hoover, W. G. Canonical dynamics—equilibrium phase-space distributions. *Phys. Rev. A* **31**, 1695–1697 (1985).
- Plimpton, S. Fast parallel algorithms for short-range molecular-dynamics. *J. Comput. Phys.* **117**, 1–19 (1995).
- Humphrey, W., Dalke, A. & Schulten, K. VMD: visual molecular dynamics. *J. Mol. Graph.* **14**, 33–38 (1996).

Acknowledgements

We are grateful to B. J. Irving for carefully reading the manuscript. G.Z. thanks the National Science Foundation of China (NSFC, grant nos 11834017 and 61888102) and the Strategic Priority Research Program of CAS (grant no. XDB30000000) for their support. M.L. thanks the ESI Fund and the OPR DE International Mobility of Researchers MSCA-IF III at CTU in Prague (no. CZ.02.2.69/0.0/0.0/20_079/0017983) for their support. L.D. gratefully acknowledges the financial support from the Academy of Finland (grant no. 3333099). D.S. thanks the support from NSFC (grant no. 61734001). K.W. and T.T. acknowledge support from the Elemental Strategy Initiative conducted by the MEXT, Japan, A3 Foresight by JSPS and the CREST (JPMJCR15F3), JST. M.L., P.N. and T.P. acknowledge support from the project Novel Nanostructures for Engineering Applications CZ.02.1.01/0.0/0.0/16_026/0008396. This work was supported by the Ministry of Education, Youth and Sports of the Czech Republic through the ϵ -INFRA CZ (ID:90140). T.P., V.E.P.C. and A.S. acknowledge support from the European Union's Horizon 2020 research and innovation program under grant agreement no. 721642: SOLUTION. The data and materials are available from the corresponding authors upon request. The authors acknowledge the use of the IRIDIS High Performance Computing Facility, and associated support services at the University of Southampton, in the completion of this work.

Author contributions

G.Z. supervised the research. M.L. performed the AFM measurements and data analysis. L.D., J.Y., S.W. and H.Y. performed the sample growth, TEM and spectroscopic characterizations. J.T. and L.G. performed TEM measurements. P.C. assisted with the AFM cantilever calibration methods. K.W. and T.T. offered BN flakes. P.N., V.E.P.C. and A.S. performed the simulations. M.L. and P.N. wrote the manuscript. T.P. and D.K. revised the manuscript. R.Y. and D.S. helped in the lab management. All the authors commented on the manuscript.

Competing interests

The authors declare no competing interests.

Additional information

Supplementary information The online version contains supplementary material available at <https://doi.org/10.1038/s41563-021-01058-4>.

Correspondence and requests for materials should be addressed to G.Z.

Peer review information *Nature Materials* thanks the anonymous reviewers for their contribution to the peer review of this work.

Reprints and permissions information is available at www.nature.com/reprints.